Boosting Mg deposition and dissolution from ionic liquids – The role of different additives for applications in Mg-ion batteries

Omar W. Elkhafif [a], Hagar K. Hassan [a,b,c,*], Motahira Hashmi [d], Nikhil Arya [d], Montaha Anjass [d,e], Timo Jacob [a,b,c,*]

[a] Institute of Electrochemistry, Ulm University, Albert-Einstein-Allee 47, 89081 Ulm, Germany
[b] Helmholtz-Institute-Ulm (HIU), Helmholtzstr. 11, 89081 Ulm, Germany
[c] Karlsruhe Institute of Technology (KIT), P.O. Box 3640, 76021 Karlsruhe, Germany
[d] Institute of Inorganic Chemistry I, Ulm University, Albert-Einstein-Allee 11, 89081 Ulm, Germany
[e] Department of Chemistry, University of Sharjah, Sharjah 27272, Sharjah, United Arab Emirates

Keywords:
Ionic liquid
Mg batteries
Co-solvent
Additives
Mg deposition
WS_2/PANI

A B S T R A C T

In this work, Mg deposition from 0.1 M $Mg(TFSI)_2$ dissolved in a hydrophobic ionic liquid (IL) is found to occur, regrettably at very high overpotential, which is accompanied by electrolyte decomposition. To address this issue, we have systematically improved the electrochemical performance of the Mg-IL system through three stages of electrolyte optimization. The first two stages involved investigating the effects of different co-solvents and Mg $(BH_4)_2$ as electrolyte additives, while the third stage comprised a detailed study of various ratios between the ionic liquid and different co-solvents to achieve an optimized system. Notably, a ratio of 1:3 MPPip-TFSI to diglyme exhibited higher cathodic and anodic currents, lower overpotential, and improved cycling stability compared to other co-solvents. Scanning electron microscopy micrographs and X-ray diffraction revealed uniform and reversible Mg deposition and dissolution. The optimized electrolyte was tested with WS_2/PANI as cathode material to validate our electrolyte system in a Mg battery application, achieving a specific capacity of 197 $mAh \bullet g^{-1}$ at 20 $mA \bullet g^{-1}$ at room temperature.

1. Introduction

Rechargeable magnesium-ion batteries (RMBs) have great potential as *post*-lithium-ion technology, owing to their abundance, high volumetric capacity, low cost, and safety compared to Li-ion batteries. However, numerous challenges persist in the development of a Mg battery, including finding electrolytes that are stable and compatible with the Mg anode as well as identifying high voltage cathodes that can accommodate the divalent Mg ions [1]. Various solvents including glymes, ionic liquids, and ethers have been investigated to achieve compatible electrolytes [2]. Although ionic liquids (ILs) offer remarkable properties such as wide electrochemical stability windows, thermal stability, high ionic conductivity, low vapor pressure, and high salt solubility, achieving reversible Mg deposition and dissolution remains challenging [3]. After the addition of Mg triflates to the ionic liquid electrolytes, Mg deposition could be realized on different substrates, while even 100 % reversibility could be realized on Ag substrates [4–7]. On the contrary, dissolving different Mg salts in miscellaneous ionic liquids did not promote any successful Mg deposition/dissolution. The difficulty for Mg deposition from ILs is related to the strong association of the salt anion with the Mg^{2+} cations [8]. In order to overcome this limitation, co-solvents are added to the ILs, in particular ethereal-based solvents such as tetrahydrofuran (THF), dimethoxyethane (DME), cyclic ether, and tetraglyme [7,9–12]. For instance, the addition of THF to the IL enhanced ionic conductivity and improved Mg deposition/dissolution reversibility [7]. Similarly, the addition of cyclic ethers has proven effective in promoting the reversibility of Mg deposition and dissolution [12]. Furthermore, adding a mixture of DME and tetraglyme to the IL enhanced the electrolyte's ionic conductivity, anodic stability, and cycling efficiency, while demonstrated good compatibility with TiO_2 and Mo_6S_8 [11]. However, the impact of using a high concentration of Li (BH_4)—equivalent to that of the Mg salt—in the optimized electrolyte is ambiguous, and requires further investigations.

On the other hand, utilizing cathode materials for RMBs with compatible reversible Mg intercalation at elevated potentials and a significant rate of cation migration for effective operation at higher

* Corresponding author at: Institute of Electrochemistry, Ulm University, Albert-Einstein-Allee 47, 89081 Ulm, Germany.
E-mail address: hagar.ibrahim@kit.edu (H.K. Hassan).

power levels remains a great obstacle towards a practical battery [13]. Meanwhile, there are three types of intercalation cathode materials reported for Mg batteries with 3D, 2D, and 1D diffusion channels. Chevrel phase, Mo_6S_8, along with spinel oxides and sulfides, *e.g.* Mn_2O_4, are known to have 3D diffusion channels [14,15]. On the other hand, layered sulfides and selenides, including WS_2, TiS_2, and $TiSe_2$, are designated for 2D diffusion channels [16]. As for polyanions such as silicates and phosphates, *e.g.* $FePO_4$, are the most common cathodes with 1D diffusion channels [17]. The sulfide structures have attracted great interest due to their favorable Mg mobility compared to slow diffusion and conversion reactions in the oxide-based structures [16]. Interestingly, WS_2 is recognized as preferred intercalation host for Mg batteries due to its weaker ionic bonds and van der Waals forces in comparison to other transition metal sulfides as well as its loosely stacked layer structure [18]. Motivated by this aspect, WS_2 was studied in different electrolytes, *i.e.* all-phenyl complex (APC) in THF, $Mg(TFSI)_2$ and $MgCl_2$ in DME, magnesium aluminium chloride complexes (MACC)-based electrolytes and $Mg(NO_3)_2{\cdot}6H_2O$ dissolved in ACN/G4 [18–20]. Additionally, polyaniline (PANI), as an inexpensive, easy-to-synthesize conductive polymer is utilized as additive to WS_2 in order to increase the interlayer distance of layered WS_2 and thus improve the ionic mobility [21,22].

Despite numerous efforts to enhance the electrochemical efficiency of ionic liquid (IL)-based electrolytes for magnesium ion batteries, a dearth of comprehensive and systematic investigations still remains. Thus, in the present study we present an inaugural systematic exploration of the influence of additives on the electrochemical performance of IL-based Mg electrolytes, examining the individual contributions of each additive and their combined synergistic effects. Additionally, we unveil the significance of the IL itself in the performance of Mg-ion batteries. Furthermore, the optimized electrolyte has been evaluated with WS_2/PANI composites as cathode material to affirm its compatibility in a full magnesium battery configuration.

2. Experimental

2.1. Chemicals

1-Methyl-1-propylpiperidinium bis(trifluoromethylsulfonyl)imide (MPPip-TFSI) was purchased from Iolitec with purity >99 % (water <100 mg·L ^{1} and halides <100 mg·L ^{1}). Magnesium(II) bis(trifluoromethanesulfonyl)imide ($Mg(TFSI)_2$, 99.5 %) was obtained from Solvionic. Additionally, monoglyme (G1) (99.5 %), diglyme (G2) (99.5 %), triglyme (G3) (≥ 98 %), tetraglyme (G4) (≥ 99 %), 1,2-difluoro benzene (98 %) and magnesium borohydride ($Mg(BH_4)_2$, 95 %) were bought from Sigma Aldrich. Further, tetrafluoroethyl tetrafluoropropyl ether (99 %) was purchased from Apollo Scientific. Diethylene glycol diethyl ether (+99 %) was obtained from Alfa Aesar. Tungsten disulfide (WS_2, 99 %), aniline (with purity ≥99.5 %) and ammonium persulfate ($(NH_4)_2S_2O_8$, ≥ 98 %) were purchased from Sigma Aldrich.

2.2. Electrolyte preparation

All solvents were dried using 4 Å molecular sieves (Sigma Aldrich) using the same procedures as described in our previous study [23]. Mg $(TFSI)_2$ was dried under vacuum at 80 °C for 16 h and $Mg(BH_4)_2$ was used as received. Mg salts were dissolved in MPPip-TFSI at 80 °C for 2 h inside the glovebox (MBRAUN LABStar) with N_2 (5.0, MTI IndustrieGase AG) and atmosphere of O_2 and H_2O ≤ 0.5 ppm. Additionally, Mg salts were dissolved with different ratios of various co-solvents (1,2-difluorobenzene (dFBn), tetrafluoroethyl tetrafluoropropyl ether (TTE), and diethylene glycol diethyl ether (DEGDE), mono-, di-, tri-, and tetraglymes) at 40 °C for 2 h inside the glovebox, and then stored inside it for further use.

2.3. Synthesis of WS_2/PANI composites

WS_2 nanosheets were produced by liquid exfoliation of WS_2 powders (1 mg• mL ^{1}) in DMF. The mixture was sonicated for 30 min. The resultant dispersions were centrifuged at 6000 rpm for 30 min. *In situ* polymerization was performed to synthesize the PANI/WS_2 composite. Solution (a) was prepared by dissolving 1 mL of 0.1 M aniline monomer in 50 mL of 1.0 M HCl and stirred well to form aniline hydroxide. WS_2 was added to the solution while continuously stirring to form a homogeneous mixture. Solution (b) was prepared by dissolving 2.5 g of ammonium persulfate [$(NH_4)_2S_2O_8$] in 50 mL of 1.0 M HCl. Polymerization was achieved by adding solution (b) to solution (a) under robust stirring for 5–6 h in an ice bath (0–5 °C). The obtained PANI/WS_2 composite was then vacuum filtered and washed with deionized water and then dried at 40 °C for 24 h. For electrode preparation, the active material (PANI/WS_2), Ketjenblack, and poly(vinylidene difluoride) (PVDF) binder with a weight ratio of 70:20:10 were homogeneously blended in *N*-methyl-2-pyrrolidine (NMP) using a planetary mixer. The slurry was coated on an aluminium foil by the doctor-blade technique. The coated foil was subsequently dried overnight under vacuum for solvent evaporation and punched into electrode discs of 12 mm diameter. The electrodes were further dried overnight at 40 °C or 70 °C under vacuum using a Büchi glass oven to get rid of humidity prior to storage in a glovebox for cell assembly. The obtained electrodes are designated as WS_2/PANI-40 and WS_2/PANI-70, respectively.

2.4. Structural characterization

X-ray data were acquired using STOE Stadi P diffractometer under the following parameters: 40 kV, 40 mA, utilizing Cu-Kα radiation (λ = 0.154 nm) in reflection mode for Mg deposition detection, while Mo-Kα radiation (λ = 0.0709 nm) was used for WS_2/PANI samples in transmission mode for the powder samples and in reflection mode for the electrodes. The electrodes were disassembled in an Ar-filled glovebox (O_2, H_2O ≤ 0.1 mg •L ^{1}) and covered with Kapton® tape to avoid air exposure. Scanning electron microscopy (SEM) micrographs and energy-dispersive X-ray spectroscopy (EDX) were conducted using the Zeiss LEO 1550VP field emission scanning electron microscope (FESEM, Carl Zeiss, Germany). To prevent exposure to air, a transfer box was employed to move samples from the glovebox to the SEM chamber.

Raman measurements were performed in a Reinshaw Raman imaging microscope, where for excitation a He—Ne laser with 532 nm and an output power of 1 % was used. The location for laser excitation and collection of the Raman spectra was monitored using a 50× objective lens. The Raman spectra of the electrodes in their original state were acquired without undergoing any further processing. Raman measurements of the cycled electrodes were performed under argon conditions. The Raman spectra were normalized (0,100) and analyzed using the Gauss model in the OriginPro 2021 software. This analysis determined the precise peak position, bandwidth, and FWHM values for each spectrum.

2.5. Electrochemical characterization

Electrochemical quartz crystal microbalance (EQCM) measurements were carried out inside the glovebox using a Pt-coated 5.0 MHz quartz crystal as working electrode having a contact area of 0.324 cm^2 inside a temperature-controlled cell set to 60 °C to overcome the high viscosity of MPPip-TFSI. Further, a Mg meshed wire as well as a pure Mg wire were used as counter and reference electrodes, respectively. A quartz crystal microbalance with dissipation (QCM-D) (Micro Vacuum, Budapest, Hungary) connected with a Gamry potentiostat (Gamry Instruments) was employed. Cyclic voltammetry (CV) was carried out in a three-electrode BOLA cell, similar to the Swagelok setup but with the outer lining being made of Teflon. A Pt foil (MaTeck GmbH, 99.9 %) with a diameter of Ø12 mm and a thickness of 0.025 mm was used as

working and counter electrodes, respectively, while a magnesium wire was used as reference electrode. Two glass fiber separators (Whatman GF/B) soaked with 140 µL of the electrolyte were used as separator between the working and the reference electrodes as well as the counter and the reference electrodes. All measurements were carried out at room temperature and after resting at open circuit voltage (OCV) for 3 h by using a BioLogic Potentiostat. For the symmetric cell investigations, magnesium sheets (HMW Hauner GmbH, 99.8 %, Ø12 mm, and 0.1 mm thick) were used as working and counter electrodes after polishing both surfaces using sandpaper to remove the oxide layer and one glass fiber separator soaked with 70 µL of (MPPip-TFSI: diglyme (1:3) + 0.1 M Mg $(TFSI)_2$ and 0.01 M $Mg(BH_4)_2$) was used between them. Additionally, in cathode material investigations, a magnesium sheet (Ø12 mm and 0.1 mm thick) after polishing with sand paper was used as counter electrode and the WS_2/PANI cathode was used as working electrode with a glass fiber separator soaked with 70 µL of (MPPip-TFSI: diglyme (1:3) + 0.1 M $Mg(TFSI)_2$ and 0.01 M $Mg(BH_4)_2$) placed between both electrodes. The cells were kept at OCV overnight and ran at room temperature.

3. Results and discussion

Mg deposition/dissolution was studied with $Mg(TFSI)_2$ salts in a MPPip-TFSI ionic liquid, which has already been proven to facilitate Mg deposition using $Mg(OTF)_2$ [4]. Upon testing different electrochemical potential windows to track any changes in the current validating the Mg deposition, no significant increase in the current was observed until reaching a potential around 2.0 *V vs.* Mg/Mg^{2+}, as shown in Fig. 1a. Deposition of Mg at such potentials may lead to the decomposition of TFSI anions. This makes Mg deposition from pure ILs highly challenging. To substantiate this assumption, the electrochemical quartz crystal microbalance (EQCM) technique was used. As shown in Fig. 1b, at around 2.0 *V vs.* Mg/Mg^{2+}, a significant increase in current density along with a change in the frequency by 500 Hz is observed, revealing changes in the mass taking place. Following the Sauerbrey equation, fluctuations in frequency are directly related to shifts in the mass of the quartz [24,25].

By using the Sauerbrey equation in combination with Faraday's law, the change in mass is calculated as shown in eq. 1.

$$\frac{M}{Z} = \frac{FA\sqrt{\rho_q \mu_q}}{2f_0^2}\frac{df}{dQ}, \tag{1}$$

where F is Faraday's constant, A is area of the quartz crystal, ρ_q and μ_q are the density and shear modulus of the quartz crystal, respectively, while f_0 is the change in resonance frequency of the crystal.

The electro reduction of Mg^{2+} ions to metallic Mg resulting in a $\frac{M}{Z}$ value of 12 g/mol. However, a higher $\frac{M}{Z}$ value of 21.8 g/mol was obtained from the Δf *vs.* Q diagram as shown in Fig. 1c. This possibly indicating another process to take place at the same potential such as the decomposition of TFSI anions or $MPPI^+$ cations [26,27]. Furthermore, as shown in Fig. 1d, the SEM micrograph illustrates the presence of inhomogeneous Mg islands. The EDS shown in the inset of Fig. 1d reveals the presence of comparable percentages of F and S that might be attributed to TFSI decomposition or the deposition of Mg-complexes.

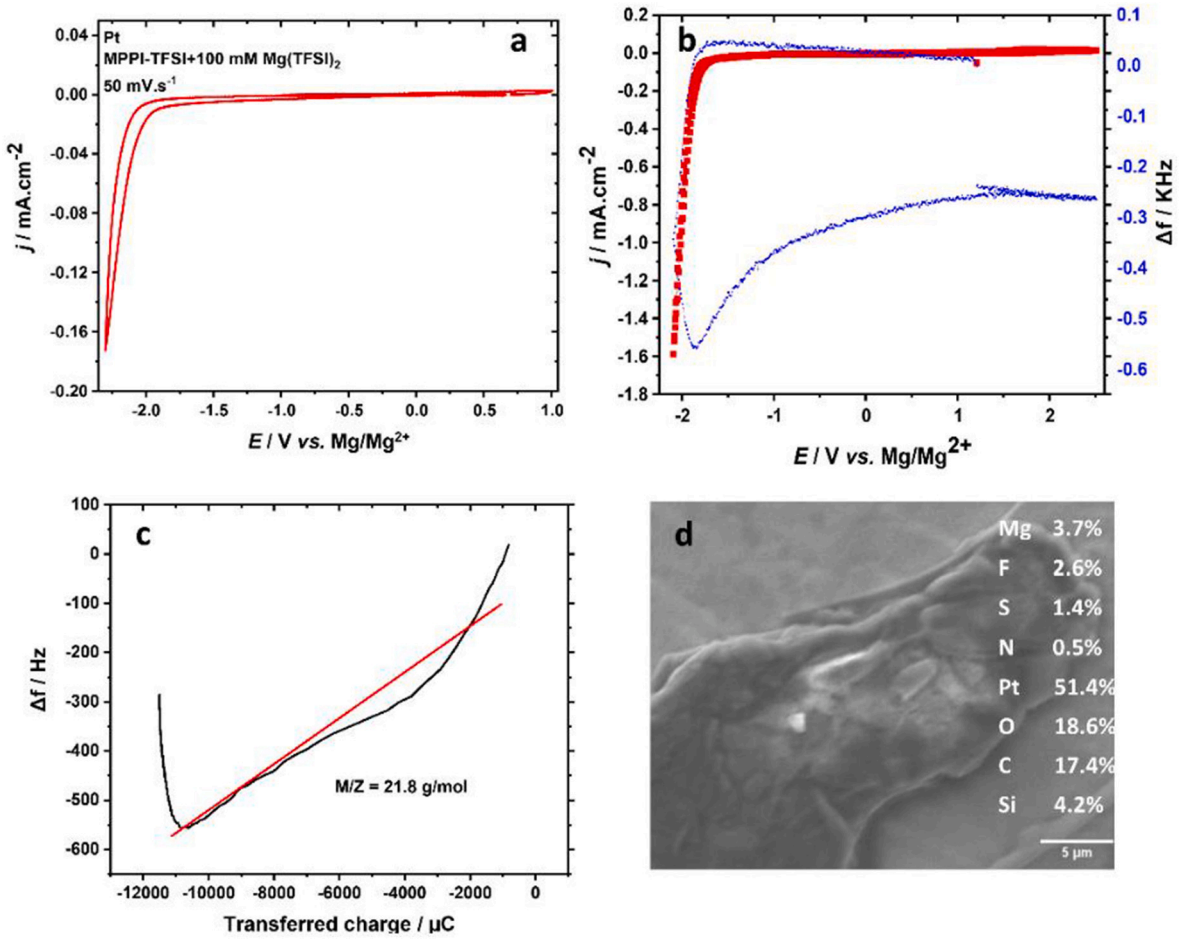

Fig. 1. a) Cyclic voltammetry of Mg deposition from 0.1 M $Mg(TFSI)_2$ in a dried MPPip-TFSI IL on a Pt working electrode at a scan rate of 50 $mV{\cdot}s^{-1}$ *vs.* Mg/Mg^{2+}, b) EQCM measurement recorded during Mg deposition, c) EQCM measurement showing the change in frequency *versus* charge during Mg deposition, and d) SEM micrograph for Mg deposition at −2.0 V *vs.* Mg/Mg^{2+} (inset: EDS data).

Therefore, we can conclude that Mg deposition from the pure ionic liquid, MPPip-TFSI, might occur accompanied by other products at very high overpotentials ≥2.0 *V*, which makes it practically infeasible.

Aiming to overcome the high overpotential of Mg deposition from IL-based electrolytes, different additives were investigated. Firstly, Mg $(BH_4)_2$ was considered as salt additive. The presence of BH_4 in the electrolyte system acts as a water scavenger as well as a complexing agent and also eliminates or diminishes the interaction between Mg and the ionic liquid components [28–31]. No significant influence was observed upon the addition of 0.01 M $Mg(BH_4)_2$ to pure MPPip-TFSI with 0.1 M $Mg(TFSI)_2$ (see Fig. S1a). A potential explanation for the limited electrochemical deposition of magnesium from ILs is their high viscosity [32,33]. Therefore, various co-solvents, such as ether-based solvents, have been explored to reduce the IL's viscosity and the overpotential as well as to obtain higher columbic efficiencies [7,9–11,34–37].

In this study, the effect of adding monoglyme in a ratio of 1:1 with MPPip-TFSI in the presence of 0.1 M $Mg(TFSI)_2$ with and without 0.01 M $Mg(BH_4)_2$ has been initially investigated, but no significant changes were observed after the addition of monoglyme. On the other hand, interestingly, upon the addition of 10 mM $Mg(BH_4)_2$, a significant change is observed (see Fig. S1b), where Mg deposits at around 0.5 *V vs.* Mg/Mg^{2+} and dissolves at around 0.2 V *vs.* Mg/Mg^{2+}. Co-solvents such as 1,2-diflurobenzene (dFBn), tetrafluoroethyl tetrafluoropropyl ether (TTE), and diethylene glycol diethyl ether (DEGDE) have been explored in combination with the ionic liquid in Li-ion batteries to investigate their impact on promoting Li^+ ion transport [38–40]. 1,2-diflurobenzene was employed to improve Li-ion transport and enhance the electrode/electrolyte interface through the formation of LiF that lead to a stable interphase [38]. On the other hand, TTE was utilized not only to reduce charge transfer impedance but also to stabilize the solid electrolyte interphase and to enhance ion conduction within the electrolyte [39]. Further, DEGDE showed good cyclic stability [38,40,41]. Therefore, in addition to the four known glymes (mono-, di-, tri-, and tetra-glymes), in our study we also selected dFBn, TTE, and DEGDE as co-solvents and analyzed their impact on Mg^{2+} ion transport. The previously mentioned co-solvents were dried with a 4 Å molecular sieve for 1 week and were afterwards added to the pre-dried MPPip-TFSI ionic liquid in a 1:1 volume ratio. Subsequently, MPPip-TFSI +0.1 M Mg $(TFSI)_2$ + 0.01 M $Mg(BH_4)_2$ was dissolved in the resulting mixture by stirring at a temperature of 40 °C for 2 h. The electrochemical performance of the resulting electrolytes has been investigated in a three-electrode setup using Pt as a working electrode (WE). As shown in Fig. 2, the effect of each co-solvent on the electrochemical performance of the IL-based electrolytes seems to be different. For instance, adding TTE as co-solvent did not alter the electrochemical performance significantly, while adding dFBn or DEGDE showed an effect on the Mg deposition feasibility as well as the Mg deposition/dissolution reversibility. In case of dFBn, magnesium deposition is observed at approximately 1.0 *V vs.* Mg/Mg^{2+}, with no dissolution detected up to 1.0 V. Thus, dFBn appears to facilitate magnesium deposition from this ionic liquid, although the dissolution process remains uncertain. Conversely, with DEGDE magnesium deposition occurs around 1.5 V *vs.* Mg/Mg^{2+}, and magnesium dissolution takes place near 0.0 V *vs.* Mg/Mg^{2+}, while during the backward scan, an ambiguous oxidation process appears at approximately –0.5 V *vs.* Mg/Mg^{2+}. Notably, DEGDE forms moderately stable complexes with magnesium ions, enhancing the reversibility of magnesium deposition and dissolution processes but still to a lesser extent compared to what has been obtained with glyme co-solvents [30]. Therefore, further investigations are needed to gain more insights into the effects of both DEGDE and dFBn, which are not within the scope of this study but will be explored in our future research endeavours.

Meanwhile, the addition of glymes to the IL resulted in a better electrochemical performance compared to the other co-solvents. Mg deposition occurs at around 0.5 *V vs.* Mg/Mg^{2+} and dissolution at around 0.1 V *vs.* Mg/Mg^{2+}. The main cause for the significant improvement is the high tendency for glymes to form Mg complexes which are not too stable compared to the co-solvents facilitating the Mg deposition/dissolution processes. Those complexes are crucial factors for improving Mg deposition/dissolution [30].

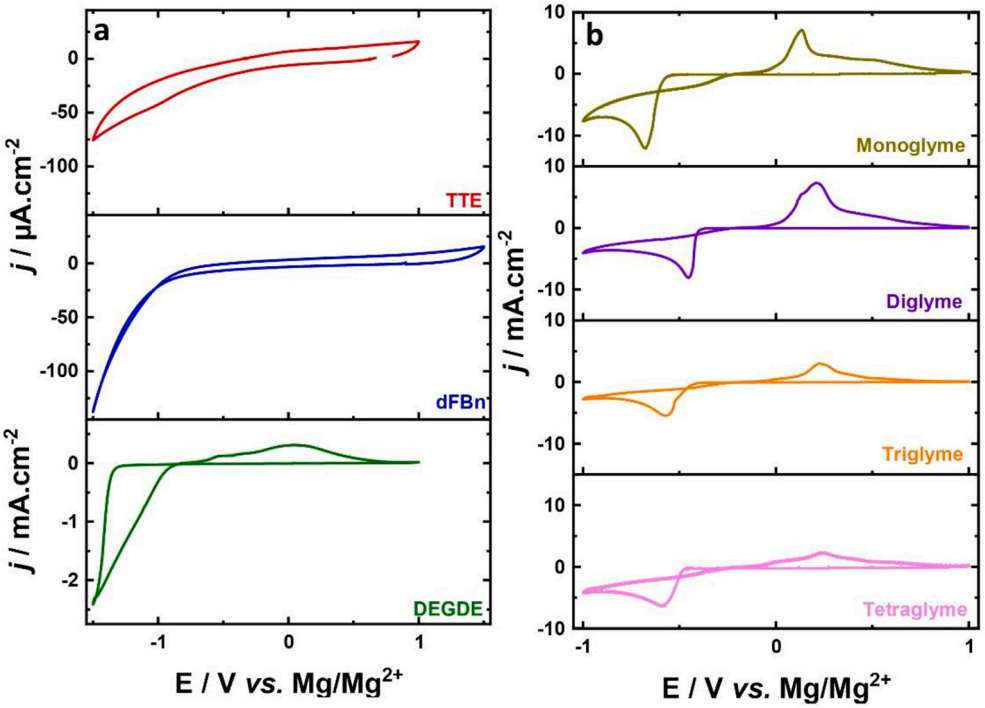

Fig. 2. Cyclic voltammograms of Mg deposition on a Pt WE from 0.1 M $Mg(TFSI)_2$ + 0.01 M $Mg(BH_4)_2$ in MPPip-TFSI IL: different co-solvents (1:1); a) tetrafluoroethyl tetrafluoropropyl ether (TTE), diflurobenzene (dFBn), and diethylene glycol diethyl ether (DEGDE), and b) monoglyme, diglyme, triglyme, and tetraglyme at a scan rate of 50 $mV \bullet s^{-1}$. *vs.* Mg/Mg^{2+}.

In the next step, a systematic study was carried out to investigate the optimum ratio of MPPip-TFSI to the different four glymes (3:1, 2:1, 1:1, 1:2, and 1:3). Fig. S2 illustrates the cyclic voltammograms for the comparison between the five ratios of MPPip-TFSI with the four glymes. From the cyclic voltammograms, four different properties affecting the electrochemical performance (such as Mg deposition overpotential, Coloumbic efficiency, anodic current peak, and cathodic current peak) were extracted and compared in histograms, as depicted in Fig. 3. Fig. 3a shows that the Mg deposition overpotential decreases with increasing the ratio of the glymes until it reaches the optimum overpotential at around 0.35 to 0.4 *V vs.* Mg/Mg^{2+}. While all different glymes have a similar impact on the Coulombic efficiency, the ratios of 1:2 and 1:3 show the highest efficiency (around 60 %), especially for G1 and G2 as shown in Fig. 3b.

Alternatively, the length of the glyme has been demonstrated to have a notable impact on both cathodic and anodic currents (see Fig. 3c and d), with the most pronounced effect at a ratio of 1:3 IL:G. This suggests that the 1:3 ratio displays a kinetic preference over 1:2. Remarkably, the length of the glyme appears to influence the Mg deposition/dissolution kinetics, where longer glyme lengths lead to slower transport kinetics in the Mg deposition and stripping.

Additionally, the 1:3 ratio exhibited the highest anodic and cathodic current peaks, while G1 and G2 showed competitive results. Therefore, concentrating on this 1:3 ratio, in the next step the different cosolvents were compared. Thus, cyclic stabilities for the 1:3 systems that contain G1 or G2 were studied. A narrower electrochemical window from 0.5 to 1.0 *V vs.* Mg/Mg^{2+} was selected to avoid any further process that may take place at potentials above 0.5 *vs.* Mg/Mg^{2+} as suggested by the subsequent increase in cathodic currents (see Fig. 2). The cyclic voltammograms for both glyme-containing systems were recorded for 50 cycles with a Pt WE at a scan rate of 50 mV/s *vs.* Mg/Mg^{2+} (see Fig. 4).

In the case of monoglyme, the cathodic currents for Mg deposition as well as the anodic current for the dissolution sharply decrease upon cycling till the cell reaches total passivation and blocking of the Mg electrode after only 20 cycles. On the other hand, the cell operated with diglyme as co-solvent showed better cyclic stability compared to monoglyme for up to 50 cycles. Following, an increase in the ratio of G1 and G2 to 4:1 was also investigated in order to check for possible enhancements. As observed in Fig. S4, the current peak for G2 is decreased compared to the 3:1 ratio, confirming again the 3:1 ratio to be optimal.

Among the other glymes, G2 stands out due to the formation of structures with different motifs compared to G1, G3, and G4. This distinction is evidently influenced by the number of oxygen atoms in the glyme chain that significantly affects the resulting Mg complexes. Two oxygen atoms (in G1) and four oxygen atoms (in G3) appear to be preferred for stabilizing solvated Mg complexes. The presence of additional oxygen atoms in G4 provides further stabilization of the structural motif initiated by G3. In contrast, G2 has three oxygen atoms, which are insufficient for full solvation in the same manner. Moreover, the ligand deficit in G2 is too small to benefit from additional G2 molecules, thereby prompting the system to create distinct structures [42]. This may elucidate the distinct electrochemical behavior of G2-based electrolytes, characterized by higher kinetics and enhanced stability. The preference of diglyme over the other glymes has also been reported in

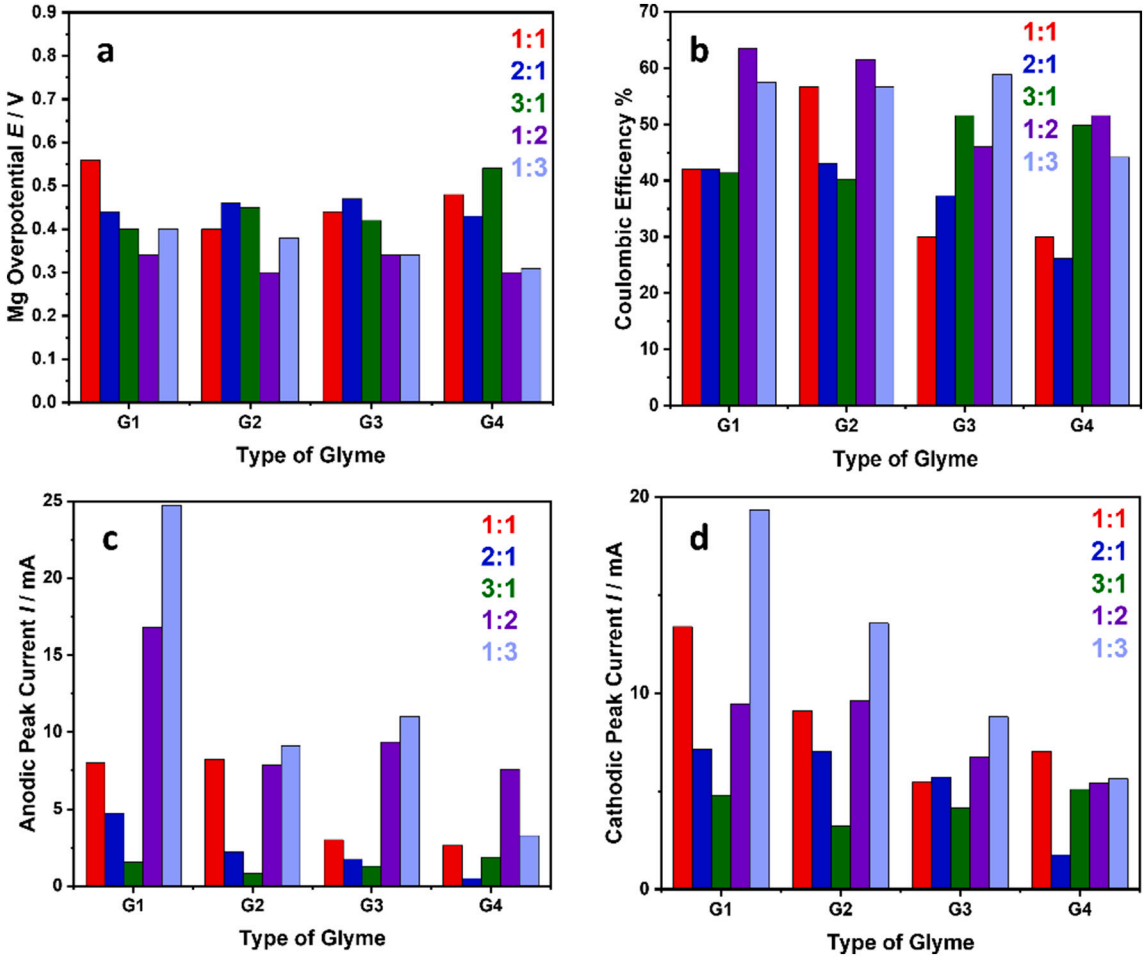

Fig. 3. Histograms, comparing the four glymes (monoglyme, diglyme, triglyme, and tetraglyme) as an additive with different ratios to MPPip-TFSI: a) overpotential of Mg deposition, b) Coulombic efficiency (in %), c) anodic current peak, and d) cathodic current peak.

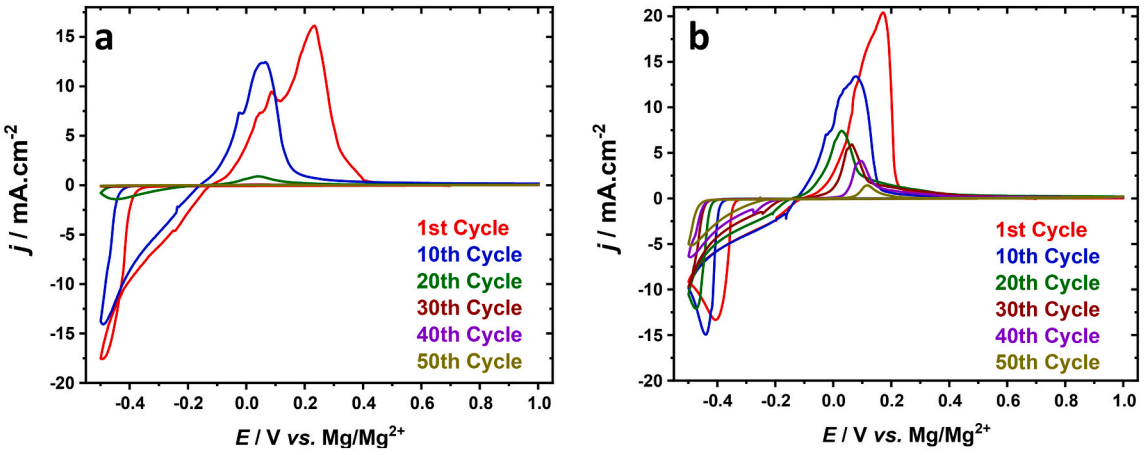

Fig. 4. Cyclic voltammograms showing the cyclic stability of Mg deposition from; a) 0.1 M $Mg(TFSI)_2$ + 0.01 M $Mg(BH_4)_2$ in MPPip-TFSI:G1 (1:3), b) 0.1 M Mg $(TFSI)_2$ + 0.01 M $Mg(BH_4)_2$ in MPPip-TFSI:G2 (1:3) with a Pt counter electrode at a scan rate of 50 mV/*s vs.* Mg/Mg^{2+}.

the literature for $Mg[Al(HFIP)_4]_2$ salts and has been attributed to the enhanced Mg^{2+} diffusivity and notable interfacial kinetics [43,44].

After the optimization of the electrolyte for Mg deposition/dissolution, scanning electron microscopy (SEM) and X-ray diffraction (XRD) were used to confirm Mg deposition and dissolution on a Pt disk. As shown in Fig. 5a, the bare Pt disk exhibits a uniform microstructure and its EDS spectra confirm its purity. After magnesium deposition at a constant current of 0.05 mA for 6 h, island-shaped magnesium deposits (29.1 wt%) were observed and confirmed by EDS analysis and elemental mapping as shown in Fig. 5b and d. Subsequently, a current of +0.05 mA was applied for another 6 h to dissolve the deposited magnesium, resulting in nearly complete dissolution where EDS shows only a 0.5 wt % residue of magnesium remaining on the surface, likely originating from the residual electrolyte (Fig. 5c). Additionally, XRD characterization was carried out for the bare Pt disk, after Mg deposition as well as after dissolution, see Fig. 5e. From the analysis of the XRD pattern, metallic Mg was deposited, which was assigned to the diffraction peaks at around 33° and 34.5° corresponding to Mg(100) and Mg(002), respectively. Furthermore, EQCM measurements were conducted and a mass of 15.16 g/mol was achieved, which is comparable to the expected mass change during Mg deposition as shown in Fig. S5.

Successively, galvanostatic cycling of a symmetric Mg cell was performed using the optimized electrolyte at 0.1 mA for 120 h, as illustrated in Fig. 6a. Initially, Mg deposition/dissolution took place at around

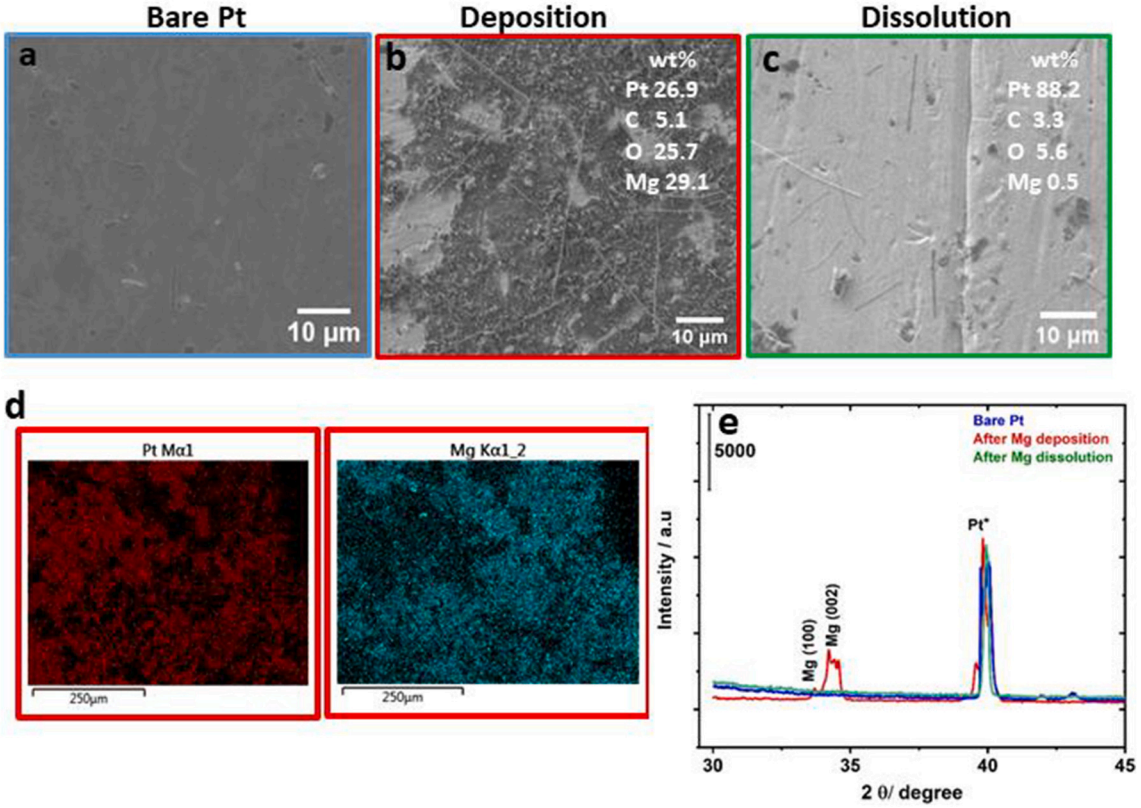

Fig. 5. SEM micrographs and EDS spectra of a) bare Pt sheet at OCV, b) after Mg deposition for 6 h at −0.05 mA, c) after Mg dissolution for 6 h at 0.05 mA from MPPip-TFSI + G2 (1:3) +0.1 M $Mg(TFSI)_2$ + 0.01 M $Mg(BH_4)_2$, d) the corresponding elemental mapping, and e) the corresponding XRD patterns for Mg deposition, dissolution and bare Pt.

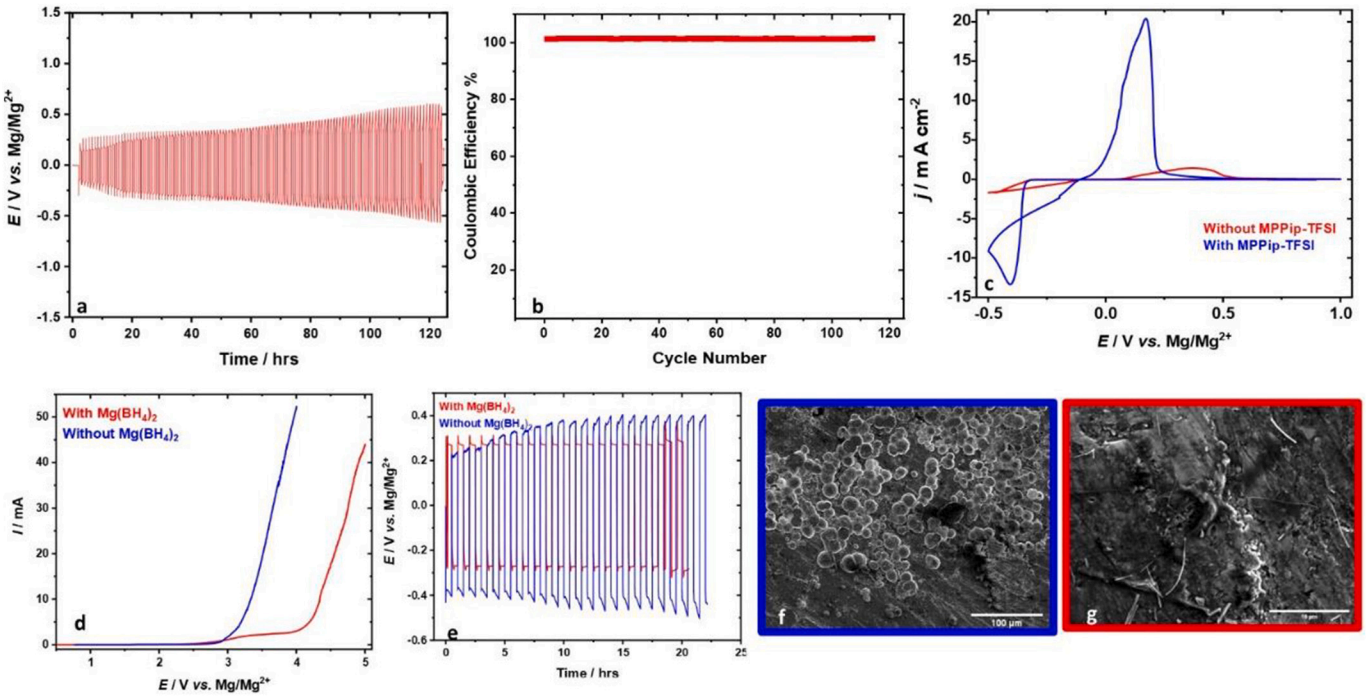

Fig. 6. a) Galvanostatic cycling of Mg symmetric cell at 0.1 mA with the optimized electrolyte for 120 cycles, b) Coulombic efficiency *vs.* number of cycles, c) CV of Mg deposition on Pt with the optimized electrolyte and in the absence of MPPip-TFSI with scan rate 50 mVs^{-1} *vs.* Mg/Mg^{2+}, d) Linear sweep voltammetry of optimized electrolyte in the presence and absence of the $Mg(BH_4)_2$, e) Influence of the presence of 0.01 M $Mg(BH_4)_2$ on the galvanostatic cycling of Mg symmetric cell at 0.05 mA, f-g) SEM micrograph for Mg deposition in the absence and presence of $Mg(BH_4)_2$ respectively.

±0.15 mV *vs.* Mg/Mg^{2+}, indicating a high stability of the optimized electrolyte in presence of the Mg anode. Additionally, the coulombic efficiency of the galvanostatic cycling was around 100 % as observed in Fig. 6b. On the other hand, the dynamic viscosity of the IL was measured after the addition of G2 in a 1:3 ratio (1 IL: 3 G2). It is observed that the dynamic viscosity of the MPPip-TFSI IL has sharply dropped from 124 to 3.22 mPa•s after the addition of G2. Lowering the viscosity of the IL-based electrolytes enhances the deposition overpotential as well as the reversibility of Mg deposition and dissolution.

From an application point of view, it was essential to investigate the role of each electrolyte component in detail, especially the highly-expensive ionic liquid. Therefore, the influence of the role of MPPip-TFSI and $Mg(BH_4)_2$ on the electrochemical performance of the suggested electrolyte was further investigated.

As shown in Fig. 6c, the presence of MPPip-TFSI results in higher kinetics, indicating the increase in current density by 10 orders of magnitude compared to the pure G2-based electrolyte. This is attributed to the inherent characteristics of the IL, such as higher ionic conductivities and low volatility compared to pure glymes.

The EIS spectra of the optimized electrolyte and in the absence of MPPip-TFSI is resembled in Fig. S6a. The solution resistance as well as the charge transfer resistance of the optimized electrolyte are very low compared to the pure diglyme was determined from fitting the EIS results using equivaled circuit shown in Fig. S6b. The results of the fitting process are shown in Table S1. The ionic conductivity values were then calculated from the solution resistances using eq. (2):

$$\sigma = \frac{L}{R.A} \tag{2}$$

where σ is the ionic conductivity, L is the distance between the electrodes (the thickness of the soaked separator), R is the solution resistance, and A is the electrode area. The calculated ionic conductivity in the presence of MPPip-TFSI is 8.53 mS cm^{-1} compared to 0.61 mS cm^{-1} in pure diglyme.

Afterwards, the role of $Mg(BH_4)_2$ was investigated in detail. Since it was previously reported that $Mg(BH_4)_2$ reduces the anodic stability [45], it was essential to study its effect on the anodic stability of the optimized electrolyte. Therefore, the anodic stability of the optimized electrolyte, with and without $Mg(BH_4)_2$, was investigated using linear sweep voltammetry (LS*V*). As shown in Fig. 6d, the optimized electrolyte exhibited anodic stability up to 4.2 V, compared to 3.0 V in its absence. This improvement can be attributed to changes in the solvation structure (complexation) in the presence of the IL-glyme mixture, compared to the pure glyme.

From the galvanostatic cycling shown in Fig. 6e, the impact of BH_4 anions become evident, reducing the overpotential of Mg deposition by 68.42 % upon addition of 10 mM. Moreover, the absence of $Mg(BH_4)_2$ altered the morphology of the deposited magnesium, as illustrated in Fig. 6e. The deposited magnesium has a spherical shape in the absence of $Mg(BH_4)_2$, compared to smooth and uniform deposit when $Mg(BH_4)_2$ is added (see Fig. 6f), suggesting a change in the nucleation and growth mechanisms of the deposited Mg.

As a proof of principle we demonstrated the performance of the optimized electrolyte in a Mg full cell, where WS_2/polyaniline (WS_2/PANI) composites were used as cathode. The integration of polyaniline (PANI) led to an enhanced ionic conductivity and suppresses restacking and agglomeration [46]. The WS_2/PANI composites were prepared as discussed in the experimental section and characterized by SEM and powder XRD. Figs. S7a and S7b show a flake-like morphology of the WS_2, while Fig. 7c represents the morphology of PANI which resembles interconnected nanofibers. The SEM picture of the WS_2/PANI composite is shown in Fig. S7d, confirming the formation of the exfoliated WS_2/PANI composite. Fig. S8 shows the XRD patterns of the WS_2 and WS_2/PANI samples, confirming the purity of WS_2 (ICSD_CollCode56014). The existence of the majority of WS_2 reflections in the WS_2/PANI pattern suggests that the composite was successfully formed. A decrease in peak positions was observed after WS_2 exfoliation in DMF and following PANi insertion, confirming an increase in the interlayer distance. The TGA analysis shown in Fig. S9 indicates that the compositions of WS_2 and

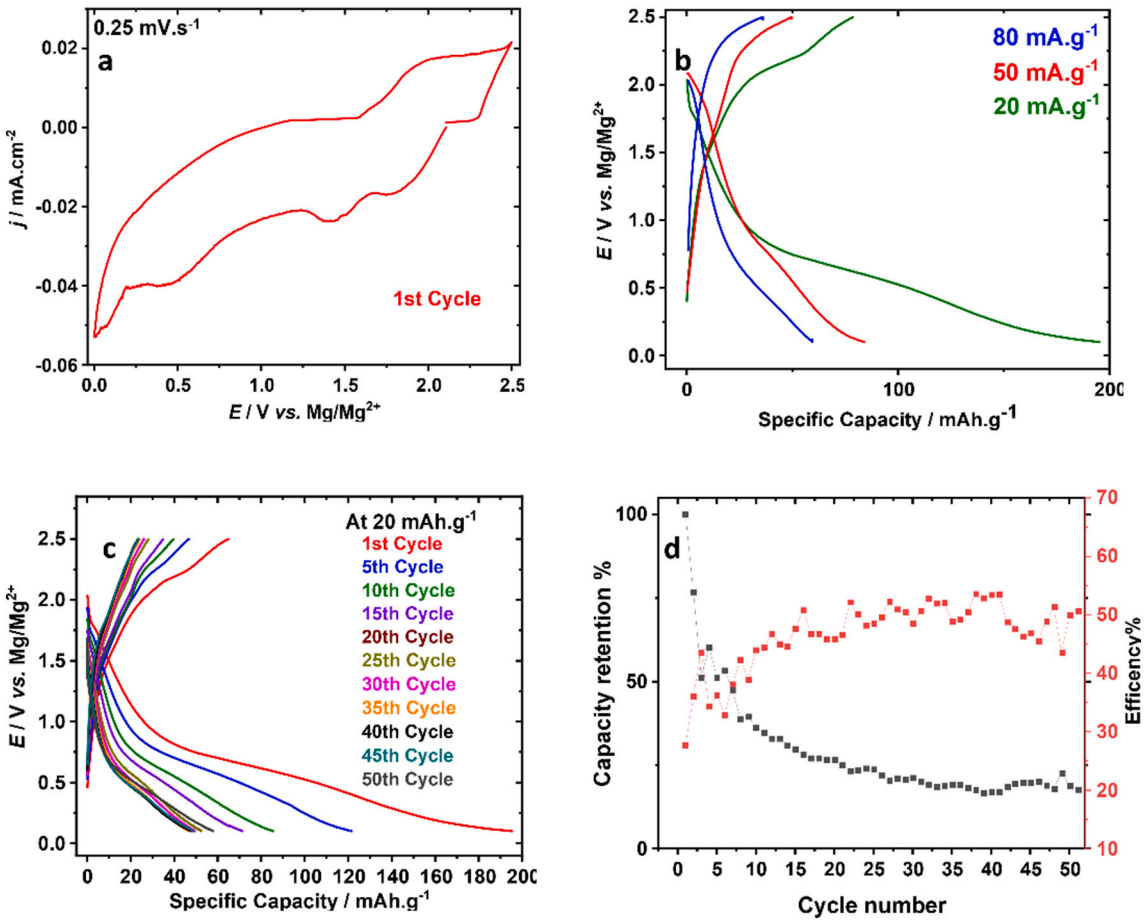

Fig. 7. a) CV of WS_2/PANI-40 | 0.1 M $Mg(TFSI)_2$+ 0.01 M $Mg(BH_4)_2$ in MPPip-TFSI IL: G2 (1:3) | Mg at scan rate 0.25 mV•s^{-1}, b) Charge–discharge profile of WS_2/PANI-40 at different specific current, c) stability of the WS_2/PANI-40 electrode up to 50 cycles at 20 mA•g^{-1}, d) Capacity retention and coulombic efficiency *vs.* number of cycles.

PANI are comparable, with 35 wt% and 46 wt% calculated for PANI and WS_2, respectively. The remaining weight is attributed to adsorbed moisture and low molecular weight PANI fragments.

The prepared WS_2/PANI composite was dried at 40 °C (labeled as WS_2/PANI-40) overnight before storing in an Ar-filled glovebox for the electrochemical measurements. Asymmetric WS_2/PANI | optimized electrolyte | Mg cells were assembled and left to rest at OCV (1.9 V) overnight. To study the intercalation and deintercalation of Mg^{2+} ions, cyclic voltammograms were recorded (at a scan rate of 0.25 mV•s ^{1}), as shown in Fig. 7a. A cathodic peak at around 0.5 V *vs.* Mg/Mg^{2+} and an anodic peak at around 2.0 V *vs.* Mg/Mg^{2+} were observed, corresponding to intercalation and deintercalation, respectively [20]. Two more cathodic peaks at 1.5 and 2.0 V *vs.* Mg/Mg^{2+} were observed which might be related to the reduction of PANI [47].

The electrochemical reaction steps during the insertion and removal of Mg^{2+} within WS_2/PANI are summarized in eqs. 3–5 [18,20,48].

$$\text{Anode}: 4\,Mg \leftrightarrow 4\,Mg^{2+} + 8e^- \quad (3)$$

$$\text{Cathode}: 6\,WS_2 + 4\,Mg^{2+} + 8e^- \leftrightarrow Mg_4W_6S_{12} \quad (4)$$

$$\text{Overall}: 6\,WS_2 + 4\,Mg \leftrightarrow Mg_4W_6S_{12} \quad (5)$$

Subsequently, the performance of WS_2/PANI-40 composites in the optimized electrolyte at different specific currents was investigated. The first cycle capacities obtained at 80, 50, and 20 mA•g ^{1} are 84, 60, 197 mAh•g ^{1}, respectively, as observed in Fig. 7b. Thus, the achieved capacity at 20 mA•g ^{1} is 2.5 times higher than what was reported with WS_2/graphene in a MAAC electrolyte [20]. Fig. 7c and d, display the cyclic stability of WS_2/PANI-40 at 20 mA•g ^{1} for 50 cycles and the capacity retention as well as the coulombic efficiency, respectively. After 50 cycles, around 25 % of the initial capacity is retained. However, the coulombic efficiency is enhanced upon cycling until it reaches 50 % at the 50th cycle. One possible reason for the low capacity retention obtained at 20 mA•g ^{1} could be attributed to the partial degradation of PANI upon cycling. Previously reported work showed that the electroactivity of PANI is influenced by the heat treatments, specifically above 70 °C [49]. To demonstrate this, WS_2/PANi was investigated after drying at 70 °C before the measurements (labeled as WS_2/PANi-70). This process induced partial degradation and cross-linking prior to our measurements. After drying the WS_2/PANI composites at 70 °C, the charge/discharge profile was investigated successively at different specific currents of 80, 50, 30, 20, 10, 8 and 5 mA·g ^{1} in the optimized electrolyte (see Fig. 8a and b). The achieved capacities in the first cycle are 2, 48, 60, 61, 600, 590 and 430 mAh·g ^{1}, respectively. The increase in capacity at a relatively low specific current (10 mA·g ^{1}) indicates a change in the charging/discharging mechanism. Further, Fig. 8c and d show the cyclic stability at 20 mA·g ^{1} and the capacity retention after 50 cycles, where 85 % of the initial capacity is retained. Surprisingly, at 20 mA·g ^{1} the initial capacity of WS_2/PANi-70 is nearly the same as the specific capacity of WS_2/PANi-40 at 25th cycle, indicating that the substantial loss in capacity is mainly attributed to the PANI partial degradation upon cycling. Surprisingly, a specific capacity of 600 mAh·g ^{1} at 10 mA·g ^{1} was achieved for the electrode dried at 70 °C. However, when the specific current is reduced to 5 mA·g ^{1}, the capacity begins to decrease instead of increasing. These results suggest that this capacity value is not solely due to Mg intercalation; it also involves

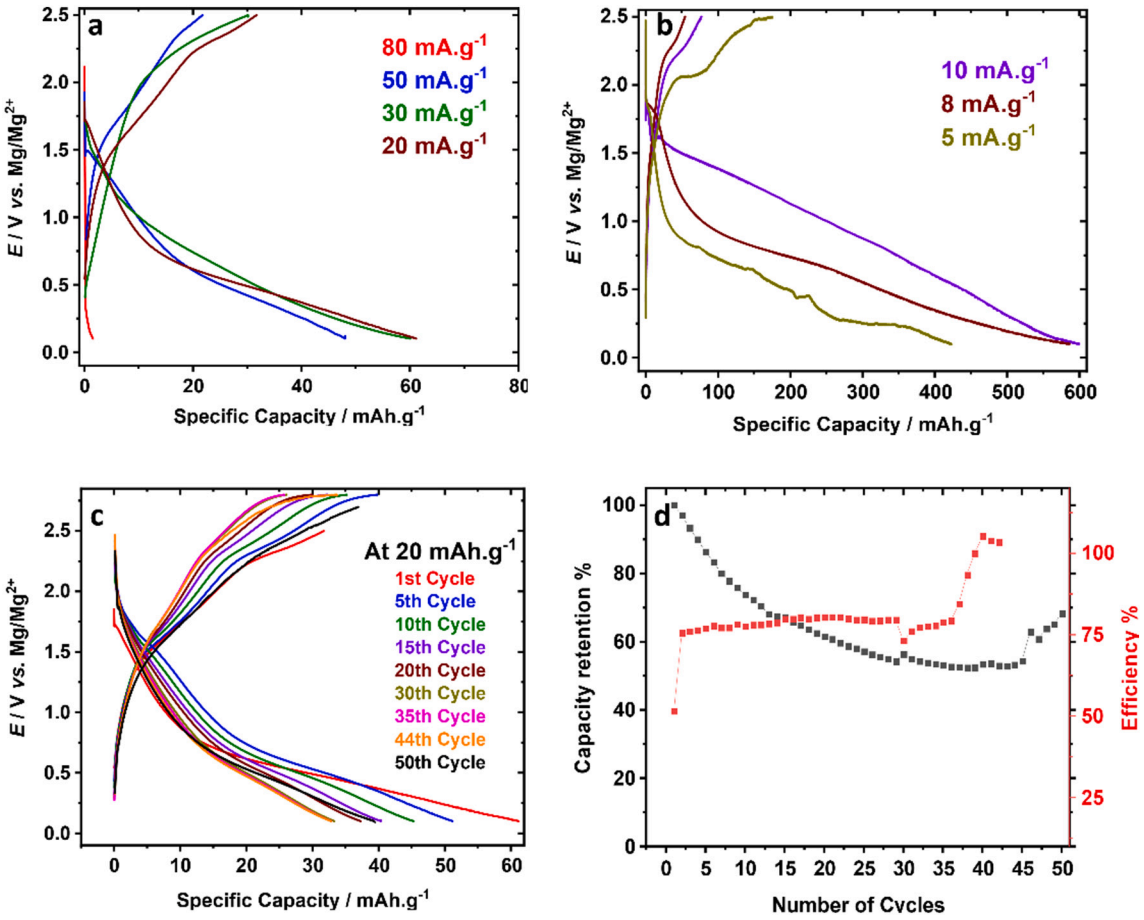

Fig. 8. a) and b) Charge–discharge profile of WS_2/ PANI-70 in 0.1 M $Mg(TFSI)_2$ + 0.01 M $Mg(BH_4)_2$ in MPPip-TFSI IL: G2 (1:3) electrolyte at different specific current (the measurements shown in b have been conducted successively), c) stability of the WS_2/PANI-70 electrode up to 50 cycles at 20 mA•g^{-1}, d) capacity retention and efficiency *vs.* number of cycles.

contributions from side reactions, such as partial polymer degradation during cycling and cross-linking. Furthermore, capacity retention decreases with increasing specific currents. This is demonstrated by <10 % capacity retention after 50 cycles at 80 mA·g ^{1}, as shown in Fig. S10. Therefore, it can be concluded that high specific currents may accelerate polymer degradation."

To further understand the intercalation and deintercalation of Mg^{2+} in the WS_2/PANI cathode and the reasons behind the capacity fading, Raman spectroscopy was performed. The Raman spectra of carbon black, WS_2/PANI-40, and WS_2/PANI-70 were examined within the frequency range of 200 to 2000 cm ^{1}, as shown in Fig. 9a. For comparison, the spectrum of the reference carbon black electrode was compared with the synthesized WS_2/PANI electrode under distinct heat treatment conditions. The reference carbon black electrode has a higher crystalline carbonaceous component, confirmed by the relative intensity bands at 1593 and 1361 cm ^{1}, corresponding to the G and D peaks, respectively [50].

The electrode incorporating WS_2/PANI has a comparable spectrum, showing prominent G and D band peaks at 1599 and 1340 cm ^{1} for the WS_2/PANI-70 electrode, and at 1606 and 1346 cm ^{1} for the WS_2/PANI-40 electrode. The apparent change in peak position might be attributed to the impact of the heat-treatment on WS_2/PANI at varying temperatures. The Raman spectra of WS_2/PANI-70 and WS_2/PANI-40 showed strong bands at around 1495 cm ^{1} and 1522 cm ^{1}, which are attributed to the C═N stretching vibrations in quinoid diimine units [51]. The red shift observed in the bands of the WS_2/PANI-70 electrode is most likely due to the cross-linking and phenazine-like structures induced by heating [51,52]. The increase in the band intensity at 1495 cm ^{1} for WS_2/PANI-70 indicates an increase in the concentration of quinoid units [51,53,54]. Nevertheless, the fluctuation in these peak intensities corresponds to potential structural alterations when the temperature rises from 40 to 70 °C (refer to Table S2 and S3) [51].

To understand the reasons behind the significant capacity fading observed with the WS_2/PANI-40 electrode, Raman spectra were also acquired during the first cycling process (Fig. 9b) at fully charged and discharged states. A small shift towards higher wavenumber was observed in almost all peaks after the discharge process due to structural alterations caused by the insertion of Mg cations. However, a shift to a higher wavenumber is observed for the C—H bending band at 1168 cm ^{1}, shifting to 1170–1173 cm ^{1} after cycling compared to the pristine electrode. This shift is associated with the transformation from quinoid to benzenoid units. An additional peak is observed at 1405 cm ^{1} after cycling and becomes pronounced after the charging process, indicating the formation of phenazine-like structures and the partial degradation as well as deprotonation of emeraldine salt [55]. The appearance of a strong band at 580 cm ^{1} after 50 successive galvanostatic cycles indicates the cross-linking of the polymer [51,54,55]. Moreover, it was difficult to distinguish the characteristic bands of WS_2 (at 350 and 420 cm ^{1}) from those of PANI at 414–418 cm ^{1}, making it challenging to comment on them.

On the other hand, SEM and XRD shown in Fig. 9c–f did not show any significant changes in the morphology or peak positions of WS_2/PANI-40 and WS_2/PANI-70 electrodes before and after cycling. These findings indicate that WS_2 preserves its structure during cycling, confirming the increase in interlayer spacing due to PANI prior to the measurements.

All these results indicate that the capacity fading observed during

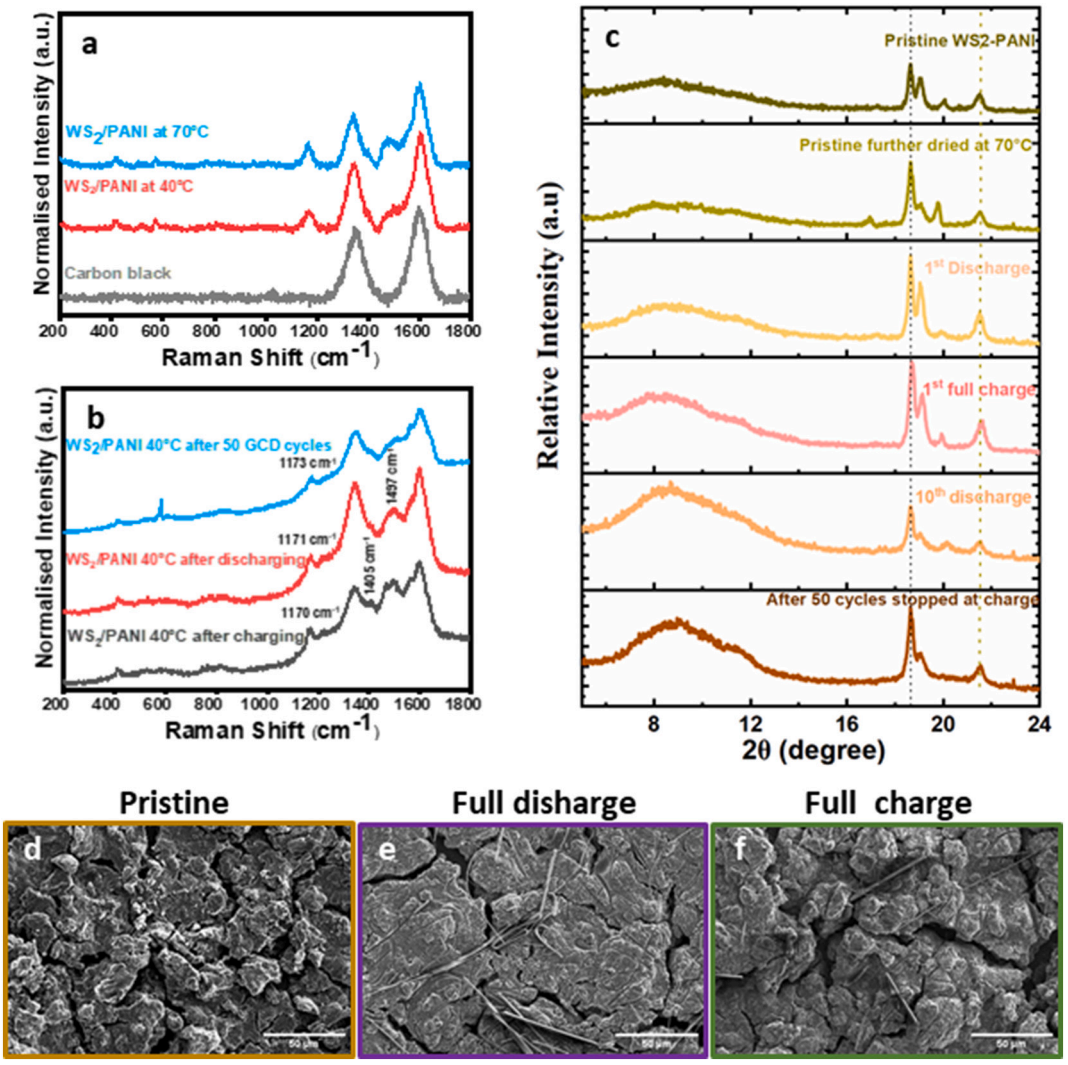

Fig. 9. a) Raman spectra of carbon black, WS_2/PANI-70 and WS_2/PANI-40 electrode, b) Raman spectra of WS_2/PAN-40 electrode at charged, at discharged state and after 50 cycles, c) XRD pattern for the pristine WS_2/PANI without any drying, pristine heat treated at 70 °C, after a full discharge, after full charge, after the 10^{th} discharge and after 50 cycles stopped after full charge all dried at 40 °C, d)-f) the corresponding SEM micrographs, respectively.

cycling of WS_2/PANI-40 is most likely attributed to the cross-linking of PANI and partial degradation during cycling. Therefore, we can conclude that the addition of PANI to the layered structure of WS_2 might expand the interlayer spacing (see Fig. S8), thereby could promote Mg diffusion during intercalation and deintercalation without altering the crystalline structure of WS_2. However, due to PANI cross-linking during cycling, alternative interlayer spacers will be explored in our future studies.

4. Conclusion

In conclusion, our electrochemical characterization using EQCM and *post-mortem* analyses highlighted the complexities and challenges of Mg deposition from pure MPPip-TFSI, which is impeded by significant electrolyte decomposition and high overpotential requirements. To address these issues, we systematically developed an optimized electrolyte system incorporating Mg salt additives and a co-solvent strategy. Among various co-solvents, glyme-based co-solvents notably enhanced electrochemical Mg deposition and dissolution. Through a detailed investigation of different co-solvent ratios, we identified that a 1:3 ratio of MPPip-TFSI to G2 yielded the highest cathodic and anodic peak currents and the lowest Mg deposition overpotential. Further analysis revealed that the ionic liquid MPPip-TFSI improved electrolyte conductivity and electrochemical kinetics, while the co-solvent reduced electrolyte viscosity, thereby lowering deposition overpotential and enhancing the reversibility of Mg deposition and dissolution. Additionally, the inclusion of $Mg(BH_4)_2$ decreased the Mg deposition overpotential by 68.42 % and allowed the use of higher current densities. As a proof of concept, this optimized electrolyte was investigated in a Mg metal battery using WS_2/PANI as cathode material. Our findings demonstrated a substantial improvement in initial capacity, achieving 197 mAh•g ^{1} at 20 mA•g ^{1}, which is 2.5 times higher than previously reported values with WS_2/graphene in a MAAC electrolyte. However, significant capacity fading of 75 % after 50 cycles at 20 mA•g ^{1} was observed, likely due to PANI cross-linking during heat treatment and subsequent cycling, in particular at higher specific currents.

CRediT authorship contribution statement

Omar W. Elkhafif: Writing – original draft, Visualization, Methodology, Investigation, Formal analysis, Data curation. **Hagar K. Hassan:** Writing – review & editing, Validation, Supervision, Methodology, Investigation, Data curation, Conceptualization. **Motahira Hashmi:** Writing – review & editing, Validation, Formal analysis. **Nikhil Arya:** Writing – review & editing, Visualization, Formal analysis. **Montaha Anjass:** Writing – review & editing, Validation, Investigation, Data

curation. **Timo Jacob:** Writing – review & editing, Validation, Supervision, Project administration, Funding acquisition.

Declaration of competing interest

The authors declare the following financial interests/personal relationships which may be considered as potential competing interests: Timo Jacob reports financial support was provided by Deutsche Forschungsgemeinschaft (DFG). Timo Jacob reports a relationship with Deutsche Forschungsgemeinschaft (DFG) that includes: funding grants. If there are other authors, they declare that they have no known competing financial interests or personal relationships that could have appeared to influence the work reported in this paper.

Acknowledgement

The authors gratefully acknowledge funding from the Deutsche Forschungsgemeinschaft (DFG) through the priority program SPP 2248 Polymer-based Batteries (Project ID 441209207) and through the individual project with ID 501805371.

Data availability

Data will be made available on request.

References

[1] R. Deivanayagam, B.J. Ingram, R. Shahbazian-Yassar, Energy Storage Materials 21 (2019) 136–153.
[2] R. Attias, M. Salama, B. Hirsch, Y. Goffer, D. Aurbach, Joule 3 (2019) 27–52.
[3] A.P. Abbott, K.J. McKenzie, Phys. Chem. Chem. Phys. 8 (2006) 4265.
[4] Y. NuLi, J. Yang, J. Wang, J. Xu, P. Wang, Electrochem. Solid-State Lett. 8 (2005) C166.
[5] P. Wang, Y. NuLi, J. Yang, Z. Feng, Surf. Coat. Technol. 201 (2006) 3783–3787.
[6] Y. NuLi, J. Yang, P. Wang, Appl. Surf. Sci. 252 (2006) 8086–8090.
[7] Q. Zhao, Y. NuLi, T. Nasiman, J. Yang, J. Wang, Int. J. Electrochem. 2012 (2012) 1–8.
[8] G. Vardar, A.E.S. Sleightholme, J. Naruse, H. Hiramatsu, D.J. Siegel, C.W. Monroe, A.C.S. Appl, Mater. Interfaces 6 (2014) 18033–18039.
[9] Z. Ma, M. Forsyth, D.R. MacFarlane, M. Kar, Green Energy & Environment 4 (2019) 146–153.
[10] W. Ren, D. Wu, Y. NuLi, X. Zhang, J. Yang, J. Wang, A.C.S. Appl, Mater. Interfaces 13 (2021) 32957–32967.
[11] S. Su, Y. NuLi, N. Wang, D. Yusipu, J. Yang, J. Wang, J. Electrochem. Soc. 163 (2016) D682–D688.
[12] I. Weber, J. Ingenmey, J. Schnaidt, B. Kirchner, R.J. Behm, ChemElectroChem 8 (2021) 390–402.
[13] A. Ponrouch, M.R. Palacín, Phil. Trans. R. Soc. A 377 (2019) 20180297.
[14] Z. Rong, R. Malik, P. Canepa, G. Sai Gautam, M. Liu, A. Jain, K. Persson, G. Ceder, Chem. Mater. 27 (2015) 6016–6021.
[15] M.D. Levi, E. Lancry, H. Gizbar, Z. Lu, E. Levi, Y. Gofer, D. Aurbach, J. Electrochem. Soc. 151 (2004) A1044.
[16] X. Sun, P. Bonnick, L.F. Nazar, ACS Energy Lett. 1 (2016) 297–301.
[17] M. Mao, T. Gao, S. Hou, C. Wang, Chem. Soc. Rev. 47 (2018) 8804–8841.
[18] W. Guo, D.A.H. Hanaor, D. Kober, J. Wang, M.F. Bekheet, A. Gurlo, Batteries 8 (2022) 116.
[19] M. Alahmadi, E. El-Dek, A. Mostafa, A. Moselhy, S. AbdelMonem, H.S. Naeer, M. Refai, X.-Y. El-Desoky, E. Sheha Yang, Tungsten Disulfide Coupling with Halogen Free Electrolyte for Magnesium Battery Applications, SSRN, 2024.
[20] M. Latha, S. Biswas, J.V. Rani, Ionics 26 (2020) 3395–3404.
[21] P. Wang, C. Tang, H. Song, L. Zhang, Y. Lu, F. Huang, ACS Appl. Mater. Interfaces 16 (2024) 14082–14092.
[22] H. Sade, J.-P. Lellouche, Nanomaterials 8 (2018) 156.
[23] O.W. Elkhafif, H.K. Hassan, M.U. Ceblin, A. Farkas, T. Jacob, ChemSusChem 16 (2023) e202300421.
[24] G. Sauerbrey, Z. Phys. 155 (1959) 206–222.
[25] D. Aurbach, M. Moshkovich, Y. Cohen, A. Schechter, Langmuir 15 (1999) 2947–2960.
[26] P.C. Howlett, E.I. Izgorodina, M. Forsyth, D.R. MacFarlane, Z. Phys. Chem. 220 (2006) 1483–1498.
[27] T. Pajkossy, C. Müller, T. Jacob, Phys. Chem. Chem. Phys. 20 (2018) 21241–21250.
[28] M. Eckardt, D. Alwast, J. Schnaidt, R.J. Behm, ChemSusChem 13 (2020) 3919–3927.
[29] M. Kar, Z. Ma, L.M. Azofra, K. Chen, M. Forsyth, D.R. MacFarlane, Chem. Commun. 52 (2016) 4033–4036.
[30] Y. Shao, T. Liu, G. Li, M. Gu, Z. Nie, M. Engelhard, J. Xiao, D. Lv, C. Wang, J.-G. Zhang, J. Liu, Sci. Rep. 3 (2013) 3130.
[31] H. Wang, X. Feng, Y. Chen, Y.-S. Liu, K.S. Han, M. Zhou, M.H. Engelhard, V. Murugesan, R.S. Assary, T.L. Liu, W. Henderson, Z. Nie, M. Gu, J. Xiao, C. Wang, K. Persson, D. Mei, J.-G. Zhang, K.T. Mueller, J. Guo, K. Zavadil, Y. Shao, J. Liu, ACS Energy Lett. 5 (2020) 200–206.
[32] N.N. Rajput, X. Qu, N. Sa, A.K. Burrell, K.A. Persson, J. Am. Chem. Soc. 137 (2015) 3411–3420.
[33] J. Drews, P. Jankowski, J. Häcker, Z. Li, T. Danner, J.M. García Lastra, T. Vegge, N. Wagner, K.A. Friedrich, Z. Zhao-Karger, M. Fichtner, A. Latz, ChemSusChem 14 (2021) 4820–4835.
[34] G.T. Cheek, W.E. O'Grady, S.Z. El Abedin, E.M. Moustafa, F. Endres, J. Electrochem. Soc. 155 (2008) D91.
[35] A. Kitada, Y. Kang, Y. Uchimoto, K. Murase, J. Electrochem. Soc. 161 (2014) D102–D106.
[36] T. Kakibe, J. Hishii, N. Yoshimoto, M. Egashira, M. Morita, J. Power Sources 203 (2012) 195–200.
[37] Y. Bi, S. He, C. Fan, J. Luo, B. Yuan, T.L. Liu, J. Mater. Chem. A 8 (2020) 12301–12305.
[38] X. Liu, A. Mariani, T. Diemant, M.E.D. Pietro, X. Dong, M. Kuenzel, A. Mele, S. Passerini, Adv. Energy Mater. 12 (2022) 2200862.
[39] H. Lu, Z. Chen, Y. Yuan, H. Du, J. Wang, X. Liu, Z. Hou, K. Zhang, J. Fang, Y. Qu, J. Electrochem. Soc. 166 (2019) A2453–A2458.
[40] S.-M. Han, J.-H. Kim, D.-W. Kim, J. Electrochem. Soc. 162 (2015) A3103–A3109.
[41] H. Lu, Z. Chen, H. Du, K. Zhang, J. Wang, Z. Hou, J. Fang, Ionics 25 (2019) 2685–2691.
[42] P. Jankowski, J.M.G. Lastra, T. Vegge, Batteries & Supercaps 3 (2020) 1350–1359.
[43] T. Mandai, Y. Youn, Y. Tateyama, Mater. Adv. 2 (2021) 6283–6296.
[44] T. Pavčnik, M. Lozinšek, K. Pirnat, A. Vizintin, T. Mandai, D. Aurbach, R. Dominko, J. Bitenc, ACS Appl. Mater. Interfaces 14 (2022) 26766–26774.
[45] X. Li, Y. Yan, T.R. Jensen, Y. Filinchuk, I. Dovgaliuk, D. Chernyshov, L. He, Y. Li, H.-W. Li, J. Mater. Sci. Technol. 161 (2023) 170–179.
[46] M. Iqbal, N.G. Saykar, P.S. Alegaonkar, S.K. Mahapatra, New J. Chem. 46 (2022) 7043–7054.
[47] A. Watanabe, K. Mori, M. Mikuni, Y. Nakamura, M. Matsuda, Macromolecules 22 (1989) 3323–3327.
[48] B. Liu, T. Luo, G. Mu, X. Wang, D. Chen, G. Shen, ACS Nano 7 (2013) 8051–8058.
[49] R. Ansari, W.E. Price, G.G. Wallace, Polymer 37 (1996) 917–923.
[50] T. Jawhari, A. Roid, J. Casado, Carbon 33 (1995) 1561–1565.
[51] J.E. Pereira da Silva, D.L.A. de Faria, S.I. Córdoba de Torresi, M.L.A. Temperini, Macromolecules 33 (2000) 3077–3083.
[52] I. Šeděnková, M. Trchová, J. Stejskal, Polym. Degrad. Stab. 93 (2008) 2147–2157.
[53] G. Ćirić-Marjanović, M. Trchová, J. Stejskal, J. Raman Spectrosc. 39 (2008) 1375–1387.
[54] J. Zhang, C. Liu, G. Shi, J. Appl. Polym. Sci. 96 (2005) 732–739.
[55] G.M. do Nascimento, M.L.A. Temperini, J. Raman Spectrosc. 39 (2008) 772–778.